nature geoscience

ARTICLES

https://doi.org/10.1038/s41561-021-00739-8

Topographic stress control on bedrock landslide size

Gen K. Li[1,2] ✉ and Seulgi Moon[1] ✉

Landslides are a major natural hazard and act as a primary driver of erosion, chemical weathering and organic carbon transfer in mountain ranges. Evaluating the impact of landslides on Earth systems requires knowledge about the controls on their size, which are not well understood. Here we show that topographic stress, resulting from the interaction between tectonic stress and topography, influences bedrock landslide size at landscape scales by modulating the subsurface material strength through fracturing and weathering. Using a three-dimensional topographic stress model, we characterize the spatial pattern of subsurface open-fracture zones in a crystalline-rock terrain of the eastern Tibetan mountains. Then, we compare the predicted open-fracture zones with 982 mapped bedrock landslides. The results show that areas with deeper subsurface open-fracture zones tend to accommodate larger landslides. This is probably due to the influences of topographically induced fractures on the material strength and groundwater flow paths and rates. We conclude that the extent of hillslope failure depends on both distant tectonic forces and local topography, which has implications for hazard mitigation, landscape evolution and the global carbon cycle.

In mountainous landscapes, bedrock landslides play an important role in hillslope erosion[1–3], chemical weathering[4], hydrological processes[5], the carbon cycle[6] and landscape evolution[7–10]. Most importantly, bedrock landslides, especially giant ones, represent a major natural hazard that threatens the safety of humans and causes severe damage to man-made infrastructure[11,12]. To better quantify landslide-driven material flux and mitigate landslide hazards, the factors that control the dimensions of bedrock landslides must be well understood.

Previous studies based on field observations suggest that bedrock material strength, largely affected by fracturing and weathering, may exert a major control on the sizes of bedrock landslides[13–18]. In addition, landslides follow power-law scaling relationships among area, depth and width, such that a landslide covering a large area tends to have a deeper failure depth and a wider width[2,19,20]. A prior study[15] inferred hillslope-scale material strength and fracture distributions by measuring seismic velocity profiles within individual hillslopes of the Southern Alps and Fiordland in New Zealand. That study[15] showed that landslides in the Southern Alps, where pervasive tectonic fractures extend deep into the subsurface, tend to be larger and deeper than those in Fiordland, where fractures relevant to geomorphic processes are restricted to within the shallow subsurface.

Theoretical and observational studies show that bedrock fracture patterns in the subsurface vary significantly due to the topographic perturbation of tectonic and gravitational stress fields[21–26]. These studies show that topographic stress fields vary as a function of tectonic stress with varying magnitude and orientation, gravitational stress and landform shapes, consequently influencing the horizontal and vertical extent of subsurface zones with open fractures in bedrock. This subsurface zone with open fractures influences various physical and chemical weathering processes and probably sets the bottom boundary for weathered bedrock[22,23,26,27]. Thus, the subsurface zone with potential open fractures (hereafter, open-fracture zone) may provide a constraint on the occurrence of bedrock landslides and limit the size of bedrock landslides. However, due to the challenges of characterizing fracture patterns on large spatial scales, few studies have directly examined landscape-scale patterns of bedrock fractures and compared them with the observed dimensions of landslides.

In this study, we examine the degree to which subsurface open-fracture zones, induced by topographic stress, affect the size of bedrock landslides at landscape scales. We investigate this relationship in a granitic terrain in the Longmen Shan at the eastern margin of the Tibetan Plateau, which features steep topography and prevalent landsliding. We first map earthquake- and precipitation-induced bedrock landslides from high-resolution satellite images and compare them with the modelled patterns of open-fracture zones from a three-dimensional topographic stress model. Our analysis demonstrates that the extent of the modelled open-fracture zones provides a strong predictor of the size of large bedrock landslides, which has broad implications for landslide hazard assessment, mountain erosion and landscape evolution.

Bedrock landslides in the eastern Tibetan mountains

The Longmen Shan in the eastern margin of the Tibetan Plateau has widespread landslides due to steep topography, monsoonal climate and active seismicity[9,12,28] (Fig. 1a). We focus our study on a crystalline-rock terrain in the central Longmen Shan, with a total area of 525 km^2 and local relief reaching up to 3 km (Fig. 1b,c). We prepared two landslide inventories, one from seismic triggering during the mainshock and aftershocks of the 2008 M_w7.9 Wenchuan earthquake, and the other one from rainfall triggering before the Wenchuan earthquake. We mapped a total of 2,828 landslides with area larger than 5,000 m^2 from 0.5 m resolution satellite images and identified landslide scars and deposit zones. The area of the largest mapped landslide was ~400,000 m^2. Then, we chose an area of 20,000 m^2 or larger for bedrock landslides, which resulted in 121 landslides triggered by precipitation and 861 triggered by the earthquake (Fig. 1d and Methods). According to a locally calibrated landslide area–depth scaling relationship[7], the depth of

[1]Department of Earth, Planetary, and Space Sciences, University of California Los Angeles, Los Angeles, CA, USA. [2]Present address: Division of Geological and Planetary Sciences, California Institute of Technology, Pasadena, CA, USA. ✉e-mail: ligen@caltech.edu; sgmoon@ucla.edu

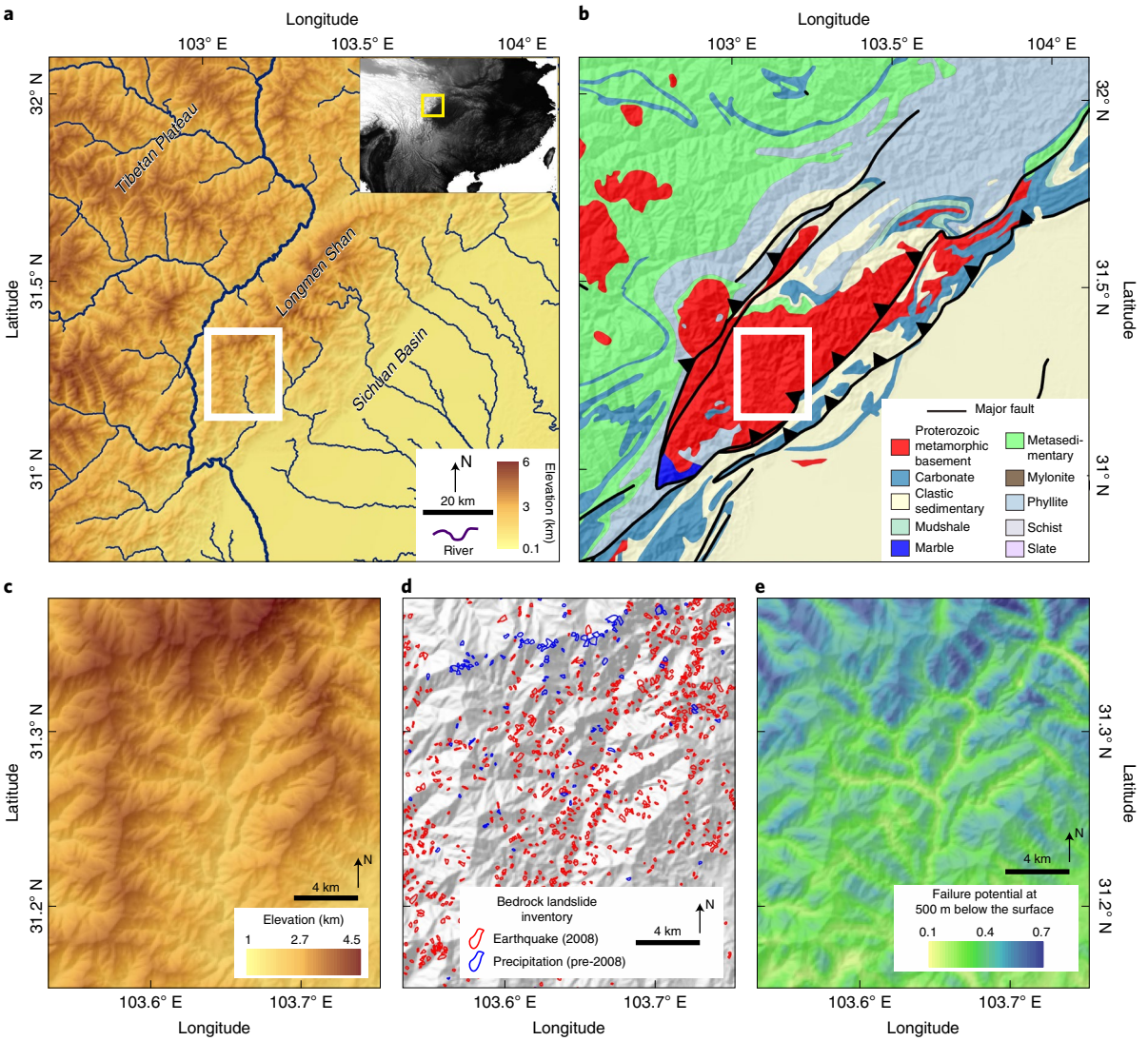

Fig. 1 | Map view of the study area. a, Elevation map of the Longmen Shan at the eastern margin of the Tibetan Plateau. The white-outlined box indicates the domain of the topographic stress model, and the inset map at the upper right shows the location of the study area in the regional context. **b**, Bedrock geology map with major faults[50,51]. **c**, Elevation map for the stress model domain. **d**, Locations of earthquake-induced (red) and precipitation-induced (blue) landslides, mapped using high-resolution satellite images from after (2008) and before (pre-2008) the M_w 7.9 Wenchuan earthquake, respectively. **e**, Spatial distribution of FP at 500 m below surface. Places with higher FP tend to have deeper open-fracture zones in the subsurface.

our mapped landslides varies from ~3 to ~20 m, and the area used to separate bedrock landslides from soil landslides corresponds to a depth of ~5 m.

Precipitation-induced landslides tend to cluster at an E–W-oriented ridge in the north, while earthquake-induced landslides occur throughout the landscapes, slightly clustered in the northeast (Fig. 1d). The proportion of precipitation-induced landslides that have large areas is greater than that of earthquake-induced landslides (Supplementary Fig. 1a,b). Both precipitation- and earthquake-induced landslides with large scar area (>40,000 m^2) tend to occur more on ridges, but there are also some in other landscape positions (Extended Data Fig. 1).

Topographic stress and predicted bedrock fracture patterns across landscapes

We modelled subsurface stress fields that account for topographic perturbation of tectonic and gravitational stress fields using the three-dimensional boundary element code Poly3D (refs. [23,26,29]) (Supplementary Information). Topographic data came from a 90 m resolution digital elevation model (DEM) and tectonic stress conditions were inferred from 23 in situ stress measurements from hydraulic fracturing (Fig. 1, Supplementary Figs. 2 and 3 and Supplementary Tables 1 and 2)[30–32]. From the modelled stress fields, we obtained the magnitudes and orientations of principal stresses: the most compressive stress (σ_{mcs}), the intermediate compressive stress (σ_{ics}), and the least compressive stress (σ_{lcs}). Then, we calculated two proxies for failure on fracture planes, that is, failure potential (FP) and σ_{lcs}, which represent the propensity of generating or reactivating shear and opening-mode fractures, respectively (Methods)[21,23]. The dimensionless quantity FP is determined by $(\sigma_{mcs} - \sigma_{lcs})/(\sigma_{mcs} + \sigma_{lcs})$. The subsurface zone, where σ_{lcs} is small or the FP is high, is expected to have more abundant fractures that are locally open, from either the generation of new fractures or the reactivation of existing fractures[23].

Then, we mapped the spatial distribution of the FP at 500 m depth (FP_{500m}), the least compressive stress at 500 m depth (LCS_{500m}) and the depth at which σ_{lcs} equals 10 MPa (D_{10MPa}) to infer the horizontal and vertical extent of the open-fracture zone. The

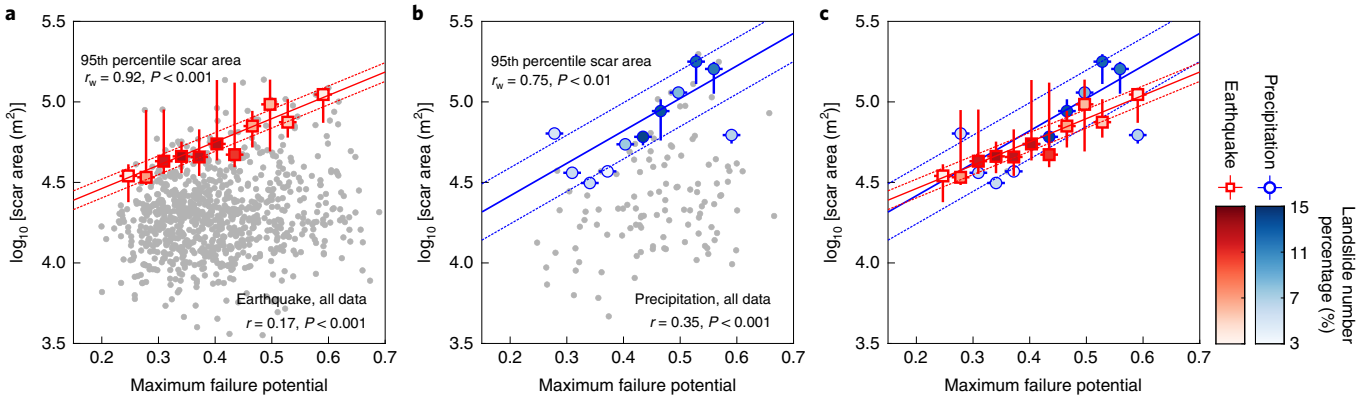

Fig. 2 | Comparison between bedrock landslide scar area and FP_{max}. a–c, The results for the earthquake-induced (**a**), precipitation-induced (**b**) and combined (**c**) bedrock landslides. Grey circles show all bedrock landslides whose entire areas are greater than 20,000 m^2. The correlation coefficient r between FP_{max} and landslide scar area is shown in the bottom right of **a** and **b**. The bedrock landslides are grouped into 16 bins with equal FP_{max} intervals ($\Delta FP_{max} = 0.031$). Red squares (**a**,**c**) and blue circles (**b**,**c**) represent the 95th percentile of scar areas from the earthquake- and precipitation-induced landslides in each bin, respectively. Vertical error bars indicate 90th and 100th percentiles. Colour saturation represents the percentage of the selected landslide number compared with total landslide numbers. We only consider an interval with greater than 3% of landslide numbers due to statistical significance. The solid line represents the fit between the 95th percentile of scar area and FP_{max}, and the dashed lines show the range of uncertainty based on the weighted root-mean-square error. The correlation coefficient r_w for the fit, weighted by the percentages of landslide numbers from each interval, is shown in the top left of **a** and **b**.

stress proxies FP and σ_{lcs} show large horizontal variations across the studied landscape in the near surface (Supplementary Fig. 4). The inferred deep open-fracture zones, based on high FP_{500m}, low LCS_{500m} and deep D_{10MPa}, mostly occur near hillslope ridges, while shallow open-fracture zones occur near valleys (Supplementary Fig. 4b–d). The FP decreases while σ_{lcs} increases with increasing depth (Supplementary Fig. 4d–f). FP_{500m} is positively correlated with both FP_{1000m} and FP_{1500m}, but to a lesser degree with FP_{1500m} (Supplementary Fig. 4g). This corroborates that the influence of topographic perturbation on stress fields is greater near the surface and diminishes with increasing depth (Supplementary Fig. 4h–i).

We find that the spatial patterns of the open-fracture zones in our study site are qualitatively similar to those from previous studies, imaged by near-surface seismic reflection and refraction methods (~60 m depth) at sites with strong tectonic compression in the eastern United States[23]. However, we acknowledge that a depth of 500 m will be deeper than that of most landslides. The choice of the 500 m depth is related to the ~350 m length of the boundary element in the stress model to accommodate our large study area and achieve a reasonable simulation time. Although 500 m is deep, the stress associated with surficial conditions has been shown to influence fracture openness to depth of ~500 m in Sweden[22]. In fact, heavily fractured granitic rocks were also observed throughout a 185-m-deep borehole from the nearby Yingxiu site[31]. Thus, we assume that the stress proxies calculated at 500 m depth can be used to represent the overall spatial patterns of open-fracture zones in the shallow subsurface (hundreds of metres of depth) affected by long wavelengths of topographic variations in the mountain range. This modelled extent of deep open-fracture zones may be sufficient to characterize the preconditioning of bedrock fracturing and weathering for large-magnitude, near-surface bedrock landslides (Methods and Supplementary Information).

We quantified the mean and maximum values of the stress proxies at 500 m depth within each landslide scar polygon and compared them with the measured sizes of bedrock landslides. The FP provides a measure of the normalized deviatoric stress that represents the potential for generating or reactivating shear fractures, which is probably related to the potential for slope failure based on the Coulomb failure rule for cohesionless material[21,33]. Thus, we focus on the relationship between FP_{500m} and landslide areas in the following discussion.

Bedrock fractures limit bedrock landslide size

Using our landslide inventory of 982 bedrock landslides, we examine the influences of the inferred open-fracture zones, induced by topographic stress, on the size of bedrock landslides. Our analysis produces several key results.

First, we find strong positive correlations between the upper bound of bedrock landslide area and the maximum value of FP_{500m} (FP_{max}) within the landslides induced by both the earthquake and precipitation. This correlation is better than the weak, but statistically significant, positive correlations between the mean and maximum values of FP_{500m} and the scar areas of all the bedrock landslides ($r = 0.17–0.35$, $P < 0.001$) (Fig. 2, grey circles). The FP_{max} value scales with the maximum extent of the open-fracture zones or the highest likelihood of generating shear fractures within the landslides. To determine the upper limit of landslide area within a given range of FP_{max}, we first measure the top 10% of bedrock landslide areas from the 90th, 95th and 100th percentiles of landslide area. We find strong positive correlations between FP_{max} and the 95th percentile of landslide area and width ($r = 0.75–0.92$, $P < 0.01$) (Fig. 2 and Supplementary Fig. 5). These strong correlations are insensitive to both the choice of an area to define bedrock landslides and the estimated uncertainties of ambient stress conditions (Supplementary Figs. 3 and 6). Other stress proxies such as the minimum value of LCS_{500m} and the maximum value of D_{10MPa} also show strong correlations with the 95th percentile of landslide area (Supplementary Fig. 5). Although we focus on the upper 10% in this analysis, we find that, in general, there are similarly good correlations between FP_{max} and the upper 20% of bedrock landslide size (Supplementary Fig. 6). This means that the extent of open-fracture zones provides a strong predictor for the upper bound of the size of large bedrock landslides.

Second, the observed relationships between landslide area and FP_{max} for earthquake- and precipitation-induced landslides largely overlap with each other (Fig. 2). This result suggests that the control of topographic stress on the upper limit of landslide size, probably by modulating material strength from fracturing and weathering, is

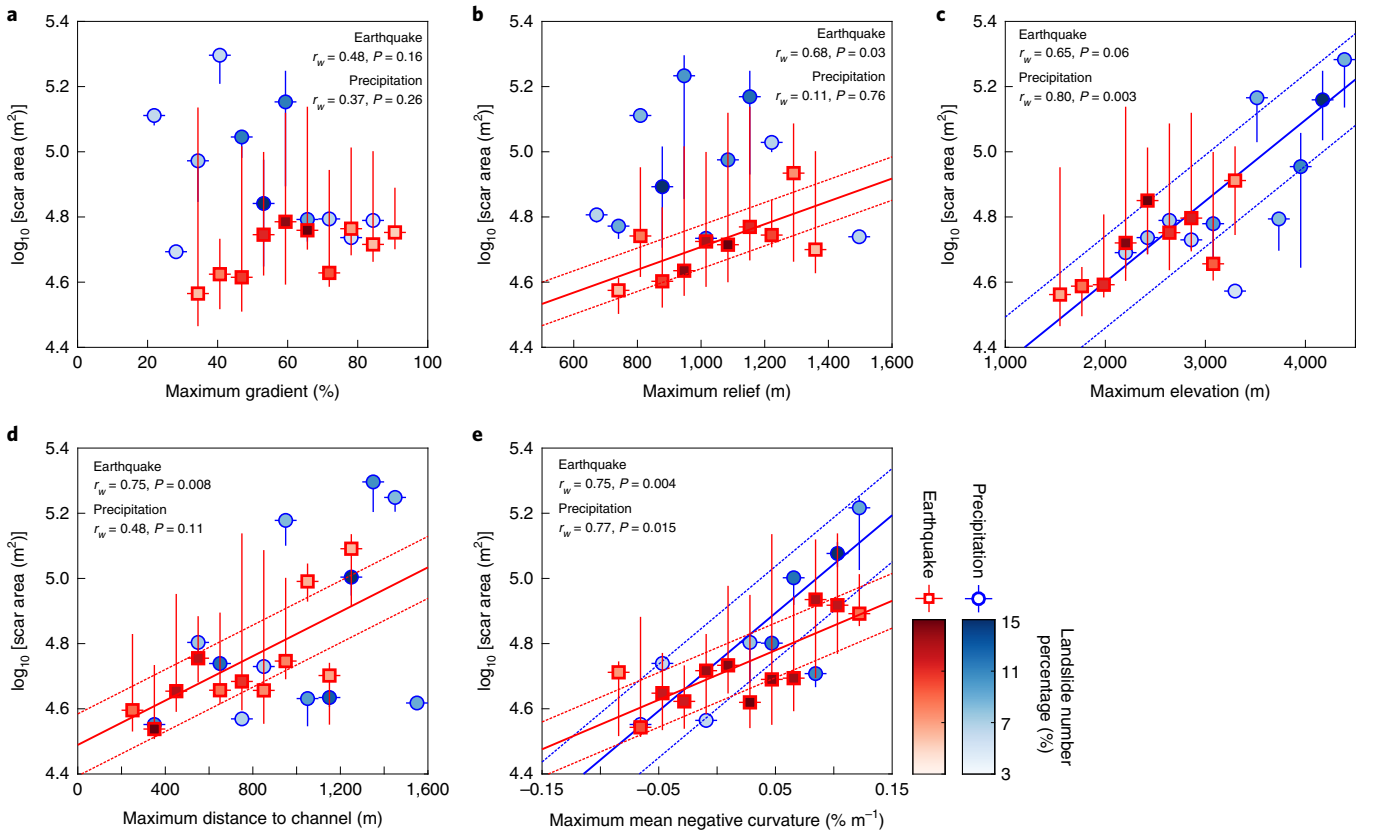

Fig. 3 | Comparison between landslide area and topographic metrics. a–e, The examined topographic metrics include the maximum topographic gradient (%) (**a**), the maximum local relief (**b**), the maximum elevation (**c**), the maximum distance to channel (**d**) and the maximum mean negative curvature (**e**). The bedrock landslides are grouped into 16 bins with equal intervals of topographic metrics. The red squares and blue circles represent the 95th percentile of scar areas from the earthquake- and precipitation-induced landslides in each bin, respectively. The solid lines represent the linear fits between the logarithms of landslide area and topographic metrics, and only the statistically significant fits with $P < 0.05$ are shown. The symbols, colours and lines have the same meaning as in Fig. 2, and the calculations of the proxies are explained in the Supplementary Information.

independent of triggering mechanisms. Interestingly, we observed that precipitation-induced landslides at our site tend to have areas larger than earthquake-induced landslides where FP_{max} exceeds ~0.4. Precipitation-induced landslides may have occurred during times wetter than the Wenchuan earthquake (12 May 2008). In this case, deep open-fracture zones may allow for deeper percolation of groundwater, increased pore pressure and higher FP_{max}, which can produce larger landslides[33].

Third, the correlations between landslide area and FP_{max} are stronger than those with the mean values of FP_{500m} (Fig. 2 and Supplementary Fig. 7). This may suggest that the weakest part of the subsurface, either from the maximum depth of open-fracture zones or with the most abundant open fractures, exerts a strong influence on landslide size rather than averaged properties. This is consistent with previous experimental studies showing that material heterogeneity (for example, weak layers from fractures or bedding) influences the size distribution of large landslides[34].

Lastly, in addition to stress proxies, we examine other potential controls on the upper limit of landslide size, which include topographic metrics (that is, gradient, local relief, mean negative curvature, elevation, and distance to channel from landslide scar)[35–38], seismic shaking proxies (that is, peak ground acceleration (PGA), PGA corrected for topographic amplification, and scar's centroid distance to fault), precipitation-related proxies (that is, mean annual precipitation rates and 90th percentile precipitation magnitudes) and a slope instability proxy that accounts for both topographic slope and subsurface hydrology[39–41] (Methods). We find that the correlations between these factors and the upper sizes of bedrock landslides are not as strong as those with stress proxies from this study (Figs. 3 and 4 and Supplementary Table 3). However, we also find that these factors show better correlations with the median size of landslides or landslide areal density than the stress proxies (for example, gradient and PGA for earthquake-induced landslides and elevation for precipitation-induced landslides). These different correlations may suggest that landslide magnitudes and areal density are probably controlled by different factors (Supplementary Figs. 8 and 9, Supplementary Table 3 and Supplementary Information).

Broader implications for Earth's surface environment

Our results demonstrate that the extent of subsurface open-fracture zones, induced by topographic stress, influences the size of large bedrock landslides in the steep eastern Tibetan mountains. These findings are consistent for both earthquake- and precipitation-induced landslides. As bedrock is exhumed, fractures start to open due to the influence of surficial conditions such as topographic perturbation on stress fields[21–23,25,26]. Open fractures in bedrock further promote percolation of fluids into and through the subsurface, enhancing physical and chemical weathering processes such as frost cracking and reactive transport[27,42,43]. Furthermore, the opening of fractures may be enhanced by subcritical crack growth induced by variations in near-surface environmental conditions[44]. While multiple mechanisms may be at play, our study shows for the first time that the extent of deep open-fracture zones induced by topographic stress governs the maximum size and depth that a bedrock landslide can reach.

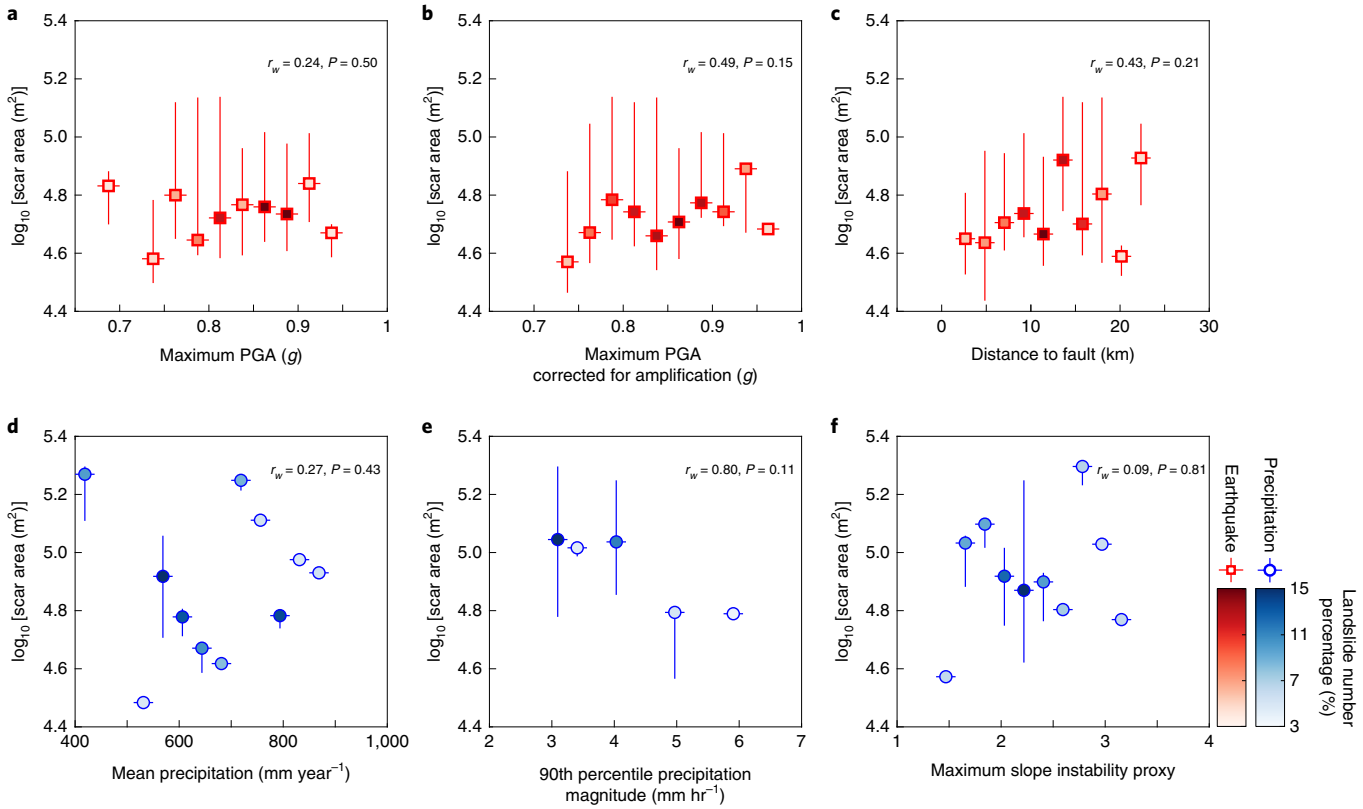

Fig. 4 | Comparison between bedrock landslide scar area and controls of seismic shaking and precipitation. a–f, Results for the seismic shaking proxies of maximum PGA (**a**), maximum PGA corrected for topographic amplification (**b**) and distance to fault (**c**) for earthquake-induced landslides, and precipitation-related metrics of mean values of mean annual precipitation rate (**d**), 90th percentile of precipitation magnitude (**e**) and maximum value of slope instability proxy (**f**) for precipitation-induced landslides. The bedrock landslides are grouped into 16 bins with equal intervals of the examined metrics and used to quantify the 95th percentile of scar areas. None of the proxies show statistically significant fits with the 95th percentile of scar areas. The symbols and colours have the same meanings as in Fig. 2, and the calculations of the proxies are explained in the Supplementary Information.

Our study highlights the important role of topographically induced bedrock fractures in landslide hazard, surface erosion and landscape evolution. This connection means that topographic development in tectonically active areas will promote spatially varying open-fracture zones in the shallow subsurface, which can facilitate large bedrock landslides in certain locations with a greater hazard magnitude. In addition, the combined effects of fractures, topography and landslide erosion may provide a negative feedback mechanism between tectonics and topographic evolution by effectively reducing topographic development in tectonically active regions[21,26]. Large bedrock landslides impact chemical weathering and organic carbon transfer[4,6] through the exposure of fresh minerals and harvest of carbon stocks on hillslopes, respectively. Therefore, our observed connection between landslide size and topographic stress provides a potential mechanism through which tectonics may influence the carbon cycle and, thus, global climate.

Though we show strong correlations between landslide area and stress proxies, we also find correlations between landslide area and other topographic metrics, such as slope, elevation and distance to channel (Fig. 3). These correlations are somewhat expected since there are moderate spatial covariations due to the topographic involvement in subsurface stress perturbation, slope stability and seismic amplification (Figs. 3 and 5). For example, landforms with more negative curvature or higher elevation (for example, ridges) can have deeper fractured zones due to greater topographic perturbations[26,45] and amplification of seismic shaking[46,47]. We find some degree of covariation between FP_{max} and other controls (Fig. 5). However, the majority of large bedrock landslides (scar area >40,000 to >100,000 m^2) occur where FP_{max} exceeds 0.4 and is higher than expected from the linear fit between FP_{max} and other controls based on all landslides (Fig. 5 and Supplementary Table 4). These results indicate that the influence of FP_{max} on landslide magnitudes is evident even in a wide range of covarying controls.

Interestingly, the areal density of earthquake-induced landslides correlates well with hillslope gradient ($r=0.56$, $P<0.001$) and PGA ($r=0.47$, $P<0.001$), consistent with previous findings[48,49]. However, there is no positive correlation between stress proxies and areal density, although stress proxies explain better the size of landslides than any of the topographic, seismic and precipitation controls (Figs. 3, 4, Supplementary Fig. 9 and Supplementary Table 3). Considering these findings, we postulate that topographically induced fractures exert a strong and positive control on the magnitudes of bedrock landslides from both rainfall and seismic triggers while other controls may contribute more to the occurrences of landslides. We speculate that topographically induced fractures may reduce subsurface material strength at deeper depths[15], promote percolation of deep groundwater in hillslopes[23] and induce localized groundwater flows near the toe of hillslopes[33]. These effects may contribute to promoting deeper and larger hillslope failures, providing a plausible explanation for our observed control of topographic stress on bedrock landslide sizes rather than landslide areal density.

Overall, our findings reveal the surface and subsurface connection between tectonic stress, topography, fractures and erosion. Topographically induced bedrock fractures not only provide a key control on landslide size but also induce a feedback mechanism between surface and subsurface processes in tectonically active

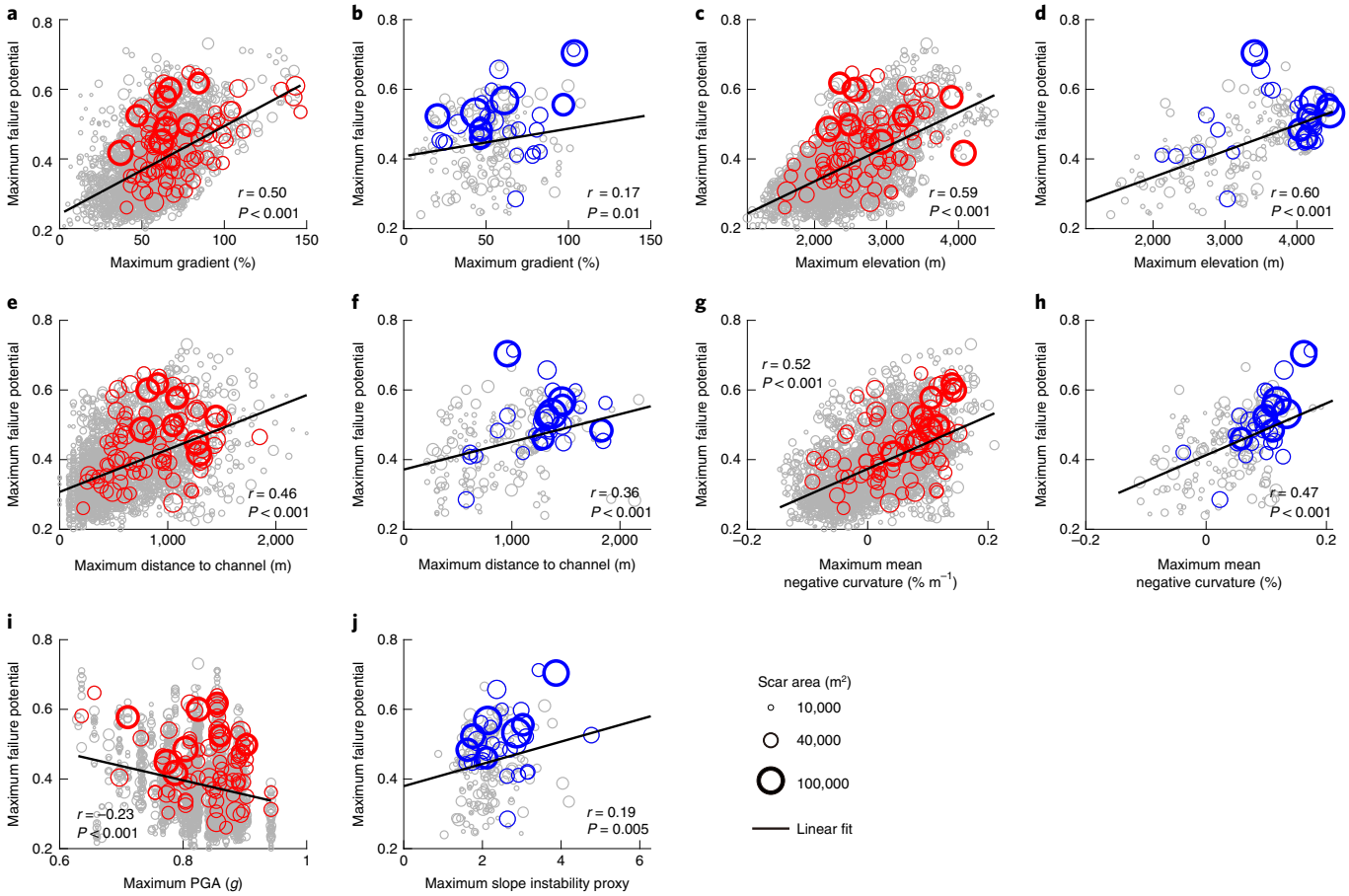

Fig. 5 | Comparison between FP_{max} and other potential controls. a–j, The results for the potential controls of maximum gradient (**a**,**b**), maximum elevation (**c**,**d**), maximum distance to channel (**e**,**f**), maximum mean negative curvature (**g**,**h**), maximum PGA (**i**) and maximum slope instability proxy (**j**) for earthquake- (**a**,**c**,**e**,**g**,**i**) and precipitation-induced (**b**,**d**,**f**,**h**,**j**) landslides. The diameter of the circles represents the scar area of landslides. Circles with grey outlines represent all landslides with entire area >5,000 m^2. Circles with thin and thick outlines represent large bedrock landslides with scar areas of 40,000–100,000 m^2 and >100,000 m^2, respectively. The solid line represents the least-squares linear fit between FP_{max} and the potential controls using all landslides. Large landslides shown by coloured circles tend to occur more in FP_{max} above the best-fit lines and where FP_{max} is higher than 0.4.

regions. Our methods can be applied to other landslide-prone settings with different environmental conditions to assess topographic stress controls on landslide sizes. Future studies comparing ground measurements and bedrock material properties, including fracture patterns and extent, in areas with contrasting tectonics will further resolve the factors that contribute to the occurrence and magnitude of landslides.

Online content

Any methods, additional references, Nature Research reporting summaries, source data, extended data, supplementary information, acknowledgements, peer review information; details of author contributions and competing interests; and statements of data and code availability are available at https://doi.org/10.1038/s41561-021-00739-8.

Received: 3 May 2020; Accepted: 18 March 2021;
Published online: 29 April 2021

References

1. Burbank, D. W. et al. Bedrock incision, rock uplift and threshold hillslopes in the northwestern Himalayas. *Nature* **379**, 505–510 (1996).
2. Houvius, N., Stark, C. P. & Allen, P. A. Sediment flux from a mountain belt derived by landslide mapping. *Geology* **25**, 231–234 (1997).
3. Korup, O. et al. Giant landslides, topography, and erosion. *Earth Planet. Sci. Lett.* **261**, 578–589 (2007).
4. Emberson, R., Hovius, N., Galy, A. & Marc, O. Chemical weathering in active mountain belts controlled by stochastic bedrock landsliding. *Nat. Geosci.* **9**, 42–45 (2016).
5. Bogaard, T. A. & Greco, R. Landslide hydrology: from hydrology to pore pressure. *Wiley Interdiscip. Rev. Water* **3**, 439–459 (2016).
6. Frith, N. V. et al. Carbon export from mountain forests enhanced by earthquake-triggered landslides over millennia. *Nat. Geosci.* **11**, 772–776 (2018).
7. Parker, R. N. et al. Mass wasting triggered by the 2008 Wenchuan earthquake is greater than orogenic growth. *Nat. Geosci.* **4**, 449–452 (2011).
8. Egholm, D. L., Knudsen, M. F. & Sandiford, M. Lifespan of mountain ranges scaled by feedbacks between landsliding and erosion by rivers. *Nature* **498**, 475 (2013).
9. Li, G. et al. Earthquakes drive focused denudation along a tectonically active mountain front. *Earth Planet. Sci. Lett.* **472**, 253–265 (2017).
10. Marc, O. et al. Long-term erosion of the Nepal Himalayas by bedrock landsliding: the role of monsoons, earthquakes and giant landslides. *Earth Surf. Dynam.* **7**, 107–128 (2019).
11. Petley, D. Global patterns of loss of life from landslides. *Geology* https://doi.org/10.1130/g33217.1 (2012).
12. Huang, R. Q. & Fan, X. M. The landslide story. *Nat. Geosci.* **6**, 325–326 (2013).
13. Schmidt, K. M. & Montgomery, D. R. Limits to relief. *Science* **270**, 617–620 (1995).
14. Clarke, B. A. & Burbank, D. W. Quantifying bedrock-fracture patterns within the shallow subsurface: Implications for rock mass strength, bedrock

landslides, and erodibility. *J. Geophys. Res. Earth Surf.* **116**, https://doi.org/10.1029/2011jf001987 (2011).
15. Clarke, B. A. & Burbank, D. W. Bedrock fracturing, threshold hillslopes, and limits to the magnitude of bedrock landslides. *Earth Planet. Sci. Lett.* **297**, 577–586 (2010).
16. Frattini, P. & Crosta, G. B. The role of material properties and landscape morphology on landslide size distributions. *Earth Planet. Sci. Lett.* **361**, 310–319 (2013).
17. Katz, O., Morgan, J. K., Aharonov, E. & Dugan, B. Controls on the size and geometry of landslides: insights from discrete element numerical simulations. *Geomorphology* **220**, 104–113 (2014).
18. Gallen, S. F., Clark, M. K. & Godt, J. W. Coseismic landslides reveal near-surface rock strength in a high-relief, tectonically active setting. *Geology* **43**, 11–14 (2015).
19. Guzzetti, F., Ardizzone, F., Cardinali, M., Rossi, M. & Valigi, D. Landslide volumes and landslide mobilization rates in Umbria, central Italy. *Earth Planet. Sci. Lett.* **279**, 222–229 (2009).
20. Larsen, I. J., Montgomery, D. R. & Korup, O. Landslide erosion caused by hillslope material. *Nat. Geosci.* **3**, https://doi.org/10.1038/ngeo776 (2010).
21. Miller, D. J. & Dunne, T. Topographic perturbations of regional stresses and consequent bedrock fracturing. *J. Geophys. Res. Solid Earth* **101**, 25523–25536 (1996).
22. Moon, S. et al. Present-day stress field influences bedrock fracture openness deep into the subsurface. *Geophys. Res. Lett.* **47**, e2020GL090581 (2020).
23. St. Clair, J. et al. Geophysical imaging reveals topographic stress control of bedrock weathering. *Science* **350**, 534–538 (2015).
24. Molnar, P., Anderson, R. S. & Anderson, S. P. Tectonics, fracturing of rock, and erosion. *J. Geophys. Res. Earth Surf.* **112**, https://doi.org/10.1029/2005jf000433 (2007).
25. Martel, S. J. Effects of small-amplitude periodic topography on combined stresses due to gravity and tectonics. *Int. J. Rock. Mech. Min. Sci.* **89**, 1–13 (2016).
26. Moon, S., Perron, J. T., Martel, S. J., Holbrook, W. S. & St. Clair, J. A model of three-dimensional topographic stresses with implications for bedrock fractures, surface processes, and landscape evolution. *J. Geophys. Res. Earth Surf.* **122**, 823–846 (2017).
27. Riebe, C. S., Hahm, W. J. & Brantley, S. L. Controls on deep critical zone architecture: a historical review and four testable hypotheses. *Earth Surf. Process. Landf.* **42**, 128–156 (2017).
28. Burchfiel, B. C. et al. A geological and geophysical context for the Wenchuan earthquake of 12 May 2008, Sichuan, People's Republic of China. *GSA Today* **18**, 5 (2008).
29. Thomas, A. L. *Poly3D:* A Three-Dimensional, Polygonal Element, Displacement Discontinuity Boundary Element Computer Program with Applications to Fractures, Faults, and Cavities in the Earth's Crust. *Master's thesis, Stanford Univ*. (1993).
30. Meng, W. et al. Characteristics and implications of the stress state in the Longmen Shan fault zone, eastern margin of the Tibetan Plateau. *Tectonophysics* **656**, 1–19 (2015).
31. Wu, M. et al. Preliminary results of in-situ stress measurements along the Longmenshan Fault zone after the Wenchuan Ms 8.0 earthquake. *Acta Geol. Sin. Engl. Ed.* **83**, 746–753 (2009).
32. Wang, C., Song, C., Guo, Q., Mao, J. & Zhang, Y. New insights into stress changes before and after the Wenchuan earthquake using hydraulic fracturing measurements. *Eng. Geol.* **194**, 98–113 (2015).
33. Iverson, R. M. & Reid, M. E. Gravity-driven groundwater flow and slope failure potential: 1. Elastic effective-stress model. *Water Resour. Res.* **28**, 925–938 (1992).
34. Katz, O. & Aharonov, E. Landslides in vibrating sand box: what controls types of slope failure and frequency magnitude relations? *Earth Planet. Sci. Lett.* **247**, 280–294 (2006).
35. Roering, J. J., Kirchner, J. W. & Dietrich, W. E. Evidence for nonlinear, diffusive sediment transport on hillslopes and implications for landscape morphology. *Water Resour. Res.* **35**, 853–870 (1999).
36. Bennett, G. L., Miller, S. R., Roering, J. J. & Schmidt, D. A. Landslides, threshold slopes, and the survival of relict terrain in the wake of the Mendocino Triple Junction. *Geology* https://doi.org/10.1130/g37530.1 (2016).
37. Jeandet, L., Steer, P., Lague, D. & Davy, P. Coulomb mechanics and relief constraints explain landslide size distribution. *Geophys. Res. Lett.* **46**, 4258–4266 (2019).
38. Medwedeff, W. G., Clark, M. K., Zekkos, D. & West, A. J. Characteristic landslide distributions: an investigation of landscape controls on landslide size. *Earth Planet. Sci. Lett.* **539**, 116203 (2020).
39. Bookhagen, B. & Burbank, D. W. Toward a complete Himalayan hydrological budget: spatiotemporal distribution of snowmelt and rainfall and their impact on river discharge. *J. Geophys. Res.* **115**, https://doi.org/10.1029/2009jf001426 (2010).
40. Montgomery, D. R. & Dietrich, W. E. A physically based model for the topographic control on shallow landsliding. *Water Resour. Res.* **30**, 1153–1171 (1994).
41. Moon, S. et al. Climatic control of denudation in the deglaciated landscape of the Washington Cascades. *Nat. Geosci.* **4**, 469–473 (2011).
42. Anderson, R. S., Anderson, S. P. & Tucker, G. E. Rock damage and regolith transport by frost: an example of climate modulation of the geomorphology of the critical zone. *Earth Surf. Process. Landf.* **38**, 299–316 (2013).
43. Rempe, D. M. & Dietrich, W. E. A bottom-up control on fresh-bedrock topography under landscapes. *Proc. Natl Acad. Sci. USA* **111**, 6576–6581 (2014).
44. Eppes, M.-C. & Keanini, R. Mechanical weathering and rock erosion by climate-dependent subcritical cracking. *Rev. Geophys.* **55**, 470–508 (2017).
45. Martel, S. J. Effect of topographic curvature on near-surface stresses and application to sheeting joints. *Geophys. Res. Lett.* **33**, https://doi.org/10.1029/2005gl024710 (2006).
46. Meunier, P., Hovius, N. & Haines, J. A. Topographic site effects and the location of earthquake induced landslides. *Earth Planet. Sci. Lett.* **275**, 221–232 (2008).
47. Maufroy, E., Cotton, F., Cruz-Atienza, V. M. & Gaffet, S. Frequency-scaled curvature as a proxy for topographic site-effect amplification and ground motion variability. *Bull. Seismol. Soc. Am.* **105**, 354–367 (2015).
48. Meunier, P., Hovius, N. & Haines, A. J. Regional patterns of earthquake-triggered landslides and their relation to ground motion. *Geophys. Res. Lett.* **34**, https://doi.org/10.1029/2007gl031337 (2007).
49. Xu, C., Xu, X., Yao, X. & Dai, F. Three (nearly) complete inventories of landslides triggered by the May 12, 2008 Wenchuan Mw 7.9 earthquake of China and their spatial distribution statistical analysis. *Landslides* **11**, 441–461 (2014).
50. Kirkpatrick, H. M., Moon, S., Yin, A. & Harrison, T. M. Impact of fault damage on eastern Tibet topography. *Geology* https://doi.org/10.1130/g48179.1 (2020).
51. Ye, T., Huang, C. & Deng, Z. Spatial database of 1:2500000 digital geologic map of People's Republic of China. *Geol. China* **44**, 19–24 (2017).

Methods

Study area. The Longmen Shan range marks the steepest margin of the Tibetan Plateau, with a sharp elevation rise greater than 5 km over a 50 km horizontal distance from the adjacent Sichuan Basin[28]. Bounded by a range of tectonically active thrust faults, the Longmen Shan was the site of the devastating 2008 M_w 7.9 Wenchuan earthquake, which triggered >60,000 landslides[51,52]. The regional climate is dominated by the East Asian monsoon, with average annual rainfall of around 1000 mm and 70–90% of the annual precipitation occurring during the monsoon season from June to September[39]. The steep topography, monsoonal climate and widespread active-seismicity-induced landslides in the Longmen Shan mean that these landslides represent a primary contribution to hillslope erosion as well as a major natural hazard[9,12].

Stress model. We focused on a 25 km × 21 km area in the central Longmen Shan range where the bedrock geology is mainly composed of crystalline rock (Proterozoic metamorphic basement) and the local relief reaches up to 3 km (Fig. 1). We modelled the three-dimensional topographic stress fields using the boundary element model Poly3D (refs. [22,23,26,29]). We used a topographic surface from SRTM 90 m DEM data and constrained the ambient stress fields based on a compilation of 23 in situ stress measurements by hydraulic fracturing at six nearby sites[30–32] (Supplementary Figs. 2 and 3). Technical details of our modelling approaches and discussions are explained in Supplementary Section S2.

From the three-dimensional topographic stress results, we calculated two scalar quantities, that is, the magnitude of σ_{lcs} and the FP, which represent two mechanisms that could act to affect the abundance of open fractures. The magnitude of σ_{lcs} is directly obtained from the results of topographic stress modelling and works as a proxy that represents the propensity of opening mode displacement on existing fractures or generating new fractures. The FP serves as a proxy for generating shear fractures or shear sliding on existing fractures, defined as $(\sigma_{mcs} - \sigma_{lcs})/(\sigma_{mcs} + \sigma_{lcs})$, where 'mcs' denotes the most compressive principal stress. A lower σ_{lcs} suggests a higher probability of open fractures that are oriented perpendicularly to the σ_{lcs}[21,53]. Because the study area has pervasive fractures based on field observations and measurements[31,54], we interpret a higher FP as indicating where shear fractures are more likely to be generated, or where existing fractures are more likely to slide and dilate[30,33].

To characterize the spatial distribution of open fracture zones, we calculated the FP and σ_{lcs} at 500 m depth below the surface (FP_{500m} and LCS_{500m}) and the depth at which $\sigma_{lcs} = 10$ MPa (D_{10MPa}). Due to the large modelled area and high computational cost, we used a ~350 m triangular mesh in the stress model. Since the boundary element model can accurately calculate stress fields one elemental length scale (~350 m) below the surface due to singularity, we select our calculated proxies at 500 m beneath the surface. We assume that these proxies provide a meaningful characterization of the spatial variation of the open-fracture zones in the shallow subsurface of mountain ranges (hundreds of metres below the surface) considering large-scale topographic variations, previous studies on subsurface stress and fractures and local observations of subsurface and subsurface bedrock fractures[22,31,54] (see the Supplementary Information for details). For reference, the depth at which σ_{lcs} equals 10 MPa is generally around 400 to 1000 m, capturing variations of the stress fields comparable to those shown by FP_{500m} and LCS_{500m}. To compare the topographic stress model results with topographic metrics from a 90 m resolution DEM, we resampled the stress model results at a 90 m resolution.

Landslide mapping and characterization. We generated two landslide inventories that represent distinct triggering mechanisms of seismicity and climate by mapping landslides from high resolution (~0.5 m) satellite imagery from Digital Globe (WorldView and QuickBird images). The inventory for post-Wenchuan landslides included landslides that occurred within 6 months following the Wenchuan earthquake. These landslides were mainly triggered by the mainshock and aftershock sequences. The other landslide inventory was generated using images collected in 2007, before the 2008 Wenchuan earthquake. We attributed the cause of the pre-2008 landslides to climatic triggers (for example, rainstorms and flooding) because the time span over which those landslides occurred was around tens to hundreds of years (Supplementary Information), and we expect minimal influences from other historical, major earthquakes in the eastern Tibetan region during this time span (for example, the 1933 Diexi earthquake and the 1976 Songpan–Pingwu earthquake[55,56]) on our landslide inventories (see the Supplementary Information for more details).

To exclude small shallow landslides occurring within soil or at the soil–bedrock boundary, we first mapped landslides with areas greater than 5,000 m² and then used an area of 20,000 m² or larger to separate bedrock landslides from soil landslides (Supplementary Information). We chose 20,000 m² based on a locally calibrated relationship between landslide area and depth[7,57], observations of soil thickness from a local study[58], predictions of soil landslide thicknesses in steep terrain in California and Switzerland[59] and a global compilation of soil and bedrock landslides[20] (Supplementary Fig. 1). We carried out a sensitivity test to examine the correlations between FP_{max} and the 95th percentiles of bedrock landslides that were separated using a range of landslide areas from 5,000 m² to 35,000 m². We demonstrated that our results are not affected by the choice of the area used to separate bedrock landslides (Supplementary Information and Supplementary Fig. 6).

With our mapping effort, we obtained 209 climatically induced landslides and 2,619 seismically induced landslides, of which 121 and 861 were bedrock landslides, respectively. To characterize landslide size, we separated the scar and deposition zones based on satellite images. The high-resolution images allowed us to identify the boundary between landslide scar and deposition zones. We delineated the full landslide polygon, including scar and deposition zones, and separated the polygon based on the identified scar and deposition boundary. The part above and below the boundary was assigned as the scar and deposition zone, respectively. Our approach provides a conservative estimate for scar area, probably a minimum, because the bottom part of the slip surface may be obscured by deposits[60]. Our scar areas encompass on average 62% of entire landslide areas, and scar and entire areas show a strong correlation ($r = 0.90$, $P < 0.0001$) (Supplementary Information). We then measured scar area and width for each landslide. We measured each separately to obtain two independent proxies for landslide size. Landslide area and width show a good correlation (Supplementary Fig. 1c). The results of the correlation between stress proxies and landslide widths and landslide entire areas are shown in Supplementary Fig. 5. Landslide mapping procedures and bedrock landslide definition, size distributions and spatial locations are explained in more details in Supplementary Section S1.

Comparison of landslide metrics versus potential controls. To examine the conditions where landslides occur, we calculated the maximum, minimum and mean values for stress model proxies and potential controls within each landslide scar zone. Our examined controls of bedrock landslide magnitude and occurrence include topographic stress, topography, seismic shaking from the Wenchuan earthquake, and precipitation rate and variability. In total, we examined 14 metrics and proxies, which include five topographic metrics (gradient, local relief calculated as the range of elevation within 1 km radius circular windows, mean negative curvature, elevation and distance to channel), three seismic shaking proxies (PGA, PGA corrected for topographic amplification from the Wenchuan earthquake and distance to fault) and three precipitation-related proxies (mean annual precipitation rates, 90th percentile precipitation magnitudes and a slope instability proxy). The PGA data were obtained from the U.S. Geological Survey Earthquake Hazard Program (https://earthquake.usgs.gov/earthquakes/eventpage/usp000g650/executive). Distance to channel is calculated as the steepest descent distance to the nearest channel within all points in a landslide scar zone. We assume that this proxy represents a landslide's accommodation space. Distance to fault is calculated as the distance from the centroid of the landslide scar to the Yingxiu-Beichuan fault[50], the main fault ruptured during the Wenchuan earthquake.

Then, we use three approaches to examine the potential controls for the sizes, abundances and locations of bedrock landslides. The approaches are based on (1) binning bedrock landslides using metric and proxy values, (2) segregating the study area into 2 km × 2 km grids and (3) analysing the covariation of controls using the whole landslide datasets. The detailed explanation for the quantification of potential controls and the statistical analysis for comparison with landslide metrics are presented in Supplementary Section S3.

Data availability

The datasets of precipitation- and earthquake-induced landslides, together with the calculated proxies, are archived at the Caltech Research Data Repository (https://doi.org/10.22002/D1.1703).

Code availability

MATLAB codes used for data analysis can be obtained from the corresponding authors upon reasonable request. Poly3D is proprietary software that can be purchased at https://www.software.slb.com.

References

52. Liu-Zeng, J., Wen, L., Oskin, M. & Zeng, L. S. Focused modern denudation of the Longmen Shan margin, eastern Tibetan Plateau. *Geochem. Geophys. Geosyst.* **12**, https://doi.org/10.1029/2011gc003652 (2011).
53. Min, K.-B., Rutqvist, J., Tsang, C.-F. & Jing, L. Stress-dependent permeability of fractured rock masses: a numerical study. *Int. J. Rock. Mech. Min. Sci.* **41**, 1191–1210 (2004).
54. Xue, Z. et al. Mesozoic crustal thickening of the Longmenshan belt (NE Tibet, China) by imbrication of basement slices: insights from structural analysis, petrofabric and magnetic fabric studies, and gravity modeling. *Tectonics* **36**, 3110–3134 (2017).
55. Huang, D., Li, Y. Q., Song, Y. X., Xu, Q. & Pei, X. J. Insights into the catastrophic Xinmo rock avalanche in Maoxian County, China: combined effects of historical earthquakes and landslide amplification. *Eng. Geol.* **258**, 105158 (2019).
56. Pei, X.-j et al. On the initiation, movement and deposition of a large landslide in Maoxian County, China. *J. Mt. Sci.* **15**, 1319–1330 (2018).

57. Whadcoat, S. K. Landsliding and Sediment Dynamics following the 2008 Wenchuan Earthquake in the Beichuan Area of China, Master's thesis, Durham Univ. (2011).
58. Zhang, J.-W. et al. Lithium and its isotopes behavior during incipient weathering of granite in the eastern Tibetan Plateau, China. *Chem. Geol.* **559**, 119969 (2021).
59. Prancevic, J. P., Lamb, M. P., McArdell, B. W., Rickli, C. & Kirchner, J. W. Decreasing landslide erosion on steeper slopes in soil-mantled landscapes. *Geophys. Res. Lett.* **47**, e2020GL087505 (2020).
60. Roback, K. et al. The size, distribution, and mobility of landslides caused by the 2015 Mw7.8 Gorkha earthquake, Nepal. *Geomorphology* **301**, 121–138 (2018).

Acknowledgements

This project was funded by NSF EAR-1945431 awarded to S.M. The authors thank S. Cui, P. van der Beek and A. Duvall for constructive reviews, and G. E. Hilley, J. J. Roering, J. T. Perron, I. J. Larsen, A. J. West, K. Shao, J. Higa, S. J. Martel, A. Yin, D. A. Paige, D. C. Jewitt and J. P. Prancevic for helpful discussions. The authors acknowledge software donations from Midland Valley Inc. and Schlumberger.

Author contributions

G.L. and S.M. conceived the study. G.L. conducted the landslide mapping. S.M. performed the topographic stress modelling, and G.L. compiled the necessary input data for the model. G.L. and S.M. analysed the results and wrote the manuscript together.

Competing interests

The authors declare no competing interests.

Additional information

Extended data is available for this paper at https://doi.org/10.1038/s41561-021-00739-8.

Supplementary information The online version contains supplementary material available at https://doi.org/10.1038/s41561-021-00739-8.

Correspondence and requests for materials should be addressed to G.K.L. or S.M.

Peer review information *Nature Geoscience* thanks Shenghua Cui, Peter van der Beek and Alison Duvall for their contribution to the peer review of this work. Primary Handling Editor: Stefan Lachowycz.

Reprints and permissions information is available at www.nature.com/reprints.

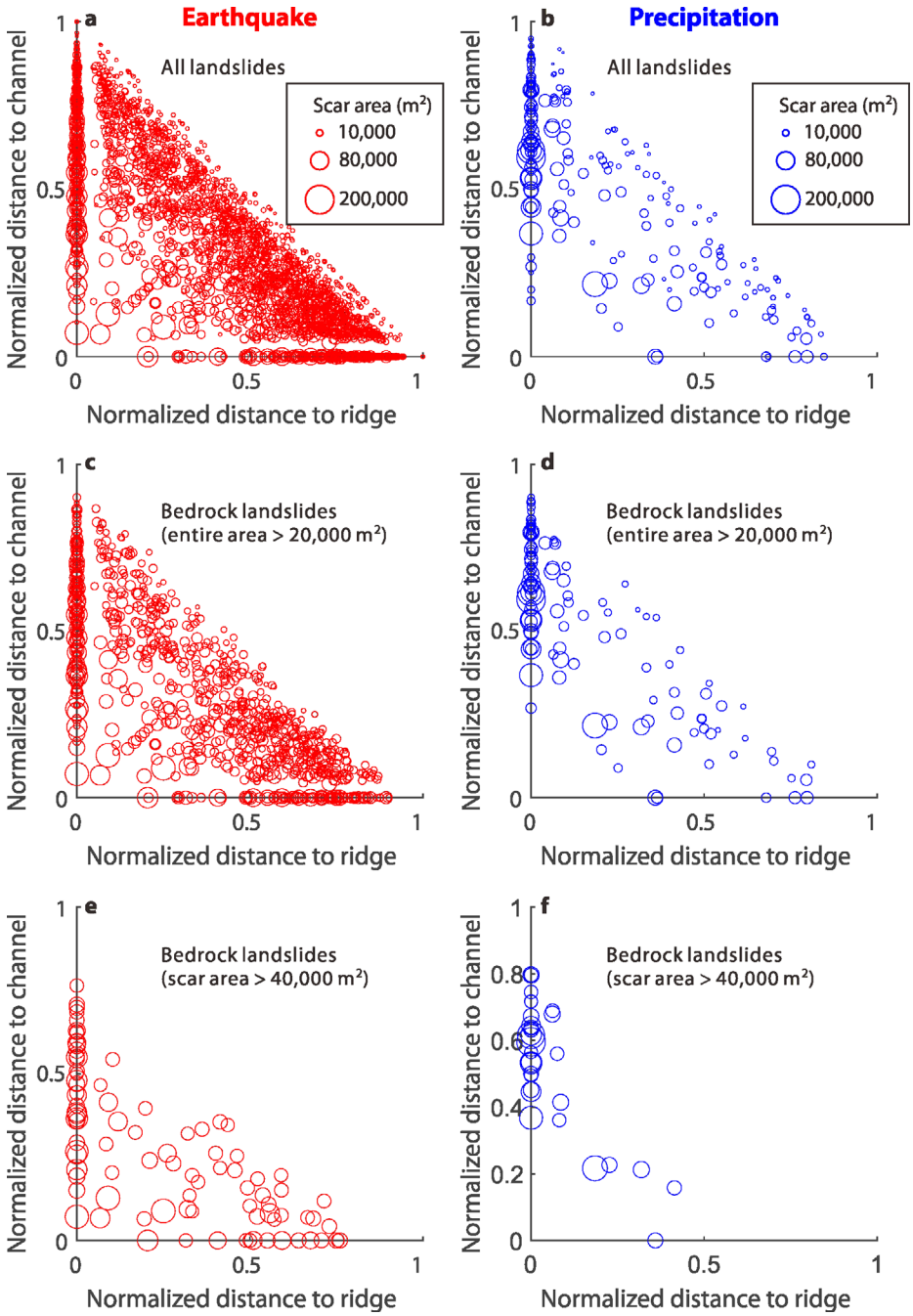

Extended Data Fig. 1 | Location of landslides with respect to ridge and channel for earthquake- and precipitation-induced landslides. a, b, All landslides with areas > 5,000 m^2, (**c, d**) bedrock landslides with areas > 20,000 m^2, and (**e, f**) large bedrock landslides with scar areas > 40,000 m^2 are shown. The distance to ridge is calculated as the steepest decent distance from the highest point of landslide scar to the nearest ridgelines, and the distance to channel is calculated as the steepest decent distance from the lowest point of landslide scar to the nearest channel following the procedure described in a previous study[46]. The distances are normalized by the total length of the hillslope in which the landslide is located. The diameters of the circles are linearly scaled with the scar areas of the landslide (Supplementary Information).